



HAL
open science

Three-phase material mapping with incomplete X-ray diffraction spectral information

Xuyang Chang, Karine Lavernhe-Taillard, Stéphane Roux, Olivier Hubert

► **To cite this version:**

Xuyang Chang, Karine Lavernhe-Taillard, Stéphane Roux, Olivier Hubert. Three-phase material mapping with incomplete X-ray diffraction spectral information. *Journal of Applied Crystallography*, 2023, 56 (3), pp.750-763. 10.1107/S160057672300331X . hal-04733736

HAL Id: hal-04733736

<https://cnrs.hal.science/hal-04733736v1>

Submitted on 12 Oct 2024

HAL is a multi-disciplinary open access archive for the deposit and dissemination of scientific research documents, whether they are published or not. The documents may come from teaching and research institutions in France or abroad, or from public or private research centers.

L'archive ouverte pluridisciplinaire **HAL**, est destinée au dépôt et à la diffusion de documents scientifiques de niveau recherche, publiés ou non, émanant des établissements d'enseignement et de recherche français ou étrangers, des laboratoires publics ou privés.

Three-phase material mapping with incomplete XRD spectral information

XUYANG CHANG,^{a*} KARINE LAVERNHE-TAILLARD,^a STÉPHANE ROUX^a AND
OLIVIER HUBERT^a

^a*Univ. Paris-Saclay/CentraleSupélec/ENS Paris-Saclay/CNRS,
LMPS - Laboratoire de Mécanique Paris-Saclay,
F-91190, Gif-sur-Yvette, France. E-mail: xuyang.chang@ens-paris-saclay.fr*

X-ray Diffraction, Shape Memory Alloy, Proper Orthogonal Decomposition

Abstract

An equiatomic Nickel-Titanium shape memory alloy specimen subjected to a uniaxial tensile loading undergoes a two-step phase transformation under stress, from Austenite to Rhombohedral phase (R-phase) and further to Martensite variants. **The pseudo-elasticity** that goes along the phase transformation induces spatial inhomogeneity. To unravel the spatial distribution of phases, in-situ XRD analyses are performed as the sample is under tensile load. However, the diffraction spectra of the R-phase, as well as potential Martensite detwinning, are not known. A novel algorithm, based on a Proper Orthogonal Decomposition, (POD), and incorporating inequality constraints, is proposed in order to map out the different phases, and simultaneously yield the missing diffraction spectral information. An experimental case study illustrates the methodology.

1. Introduction

X-ray diffraction (XRD) is a popular non-destructive qualitative and quantitative technique aiming at characterizing crystal lattice parameters (Drickamer *et al.*, 1967), local strain (Gailhanou *et al.*, 2007), **microstructure evolution (Oliveira *et al.*, 2022)** or phase constituents proportions (Peng *et al.*, 2005) from analyzed specimens (*e.g.*, metals, polymers and ceramics). Although X-ray diffraction has been primarily emphasized as an efficient tool for qualitative analyses, it is often used to perform quantitative measurements of all phase concentrations within the material. Rietveld refinement method (McCusker *et al.*, 1999) is generally applied to conduct quantitative analysis of X-ray diffraction patterns. This method, however, requires the diffraction profiles for all possible phase constituents to be collected appropriately during the preparation stage, so that the individual components can be adequately identified afterward. From a practical point of view, this preparation is rather delicate for (complex) heterogeneous specimens. Moreover, the preferred-orientation effects of X-ray diffraction measurement (Dickson, 1969; Campbell Roberts *et al.*, 2002) are extremely delicate to be dealt with experimentally.

A metallic specimen, with a pronounced preferred-orientation — especially with a flat-plate geometry — may exhibit a strong $\{hkl\}$ intensity dependency when compared to theoretical powder diffraction patterns. Although many Rietveld refinement software/programs allow for the identification of an artificial preferred-orientation parameter with respect to a specific crystallographic vector based on either the March model (Dollase, 1986) or the Generalized Spherical Harmonic model (Sitepu *et al.*, 2005), it remains a crude approximation when assessing heterogeneous multi-phase specimens.

In this work, a Proper Orthogonal Decomposition (POD) algorithm, suitably extended to incorporate inequality constraints, such as positivity, (and referred to as positive-POD or p-POD) is proposed to circumvent the aforementioned challenges: for all phase constituents whose diffraction profiles are experimentally available (and denoted as 'the known con-

stituents'), the POD technique (Chatterjee, 2000) is first applied to construct the experimental diffraction spectrum while taking the preferred-orientation effect into account. Then, by enforcing the positivity constraints, the phase concentrations for 'the known constituents' can be estimated, through a quadratic minimization with convex positive constraints using the sub-gradient projection algorithm (Boyd *et al.*, 2003). Finally, the phase concentration and experimental diffraction data for the unknown constituents can be obtained.

The performance of the proposed algorithm is illustrated using a strip-shaped specimen made of equiatomic Nickel-Titanium shape memory alloy (NiTiNol) subjected to a uniaxial tensile load. Under stress, the Nickel-Titanium alloys are frequently reported to introduce a two-step martensitic phase transformation in forms of strain localization bands at ambient temperature (from Austenite (**A**) to Rhombohedral (**R**) and further to Martensite (**M**)) (Miyai *et al.*, 2006; Halani *et al.*, 2013; Stebner *et al.*, 2015).

At a given load, the X-rays diffraction profiles are recorded scanning through the specimen along the tensile direction, *i.e.*, across the strain localization bands so as to elucidate the on-going phase transformation(s) from the progressive changes in diffraction spectra. For NiTi SMA, depending on the forming process and chemical composition, when subjected to mechanical loads, ~~the~~ R-phase sometimes appears as an intermediate phase in a two-step phase transformation. It usually co-exists with Austenite at the macroscopic scale (whatever ~~the~~ stress or thermal loads) which impedes the measurement of individual diffraction spectrum. In contrast, it is possible to find specific conditions ~~under~~ which pure Austenite or Martensite phase exist in the specimen.

Moreover, the formation of strain localization bands is a macroscopic outcome of the "Martensite detwinning" process (Ng & Sun, 2006) (or the so-called "Martensite variants selection"), resulting in a pronounced preferred orientation effect.


The missing R-phase diffraction pattern and the undetermined preferred-orientation of Martensite variants prevents the Rietveld refinement method to achieve any comprehensive

results. To overcome this limitation, the proposed p-POD algorithm permits to estimate the concentration of different phases along the sample and provide an estimated R-phase diffraction spectrum. The proposed method is extremely versatile since it requires neither the complete knowledge of diffraction data for all constituents nor a delicate experimental processing to remove the signature of preferred orientations in the specimen.

The paper is organized as follows: Section 2 presents the in-situ XRD-DIC combined measurement setups and the associated strain fields and raw diffraction spectra acquired during 1D tensile loads. *The Rietveld processing method is recalled briefly in Section 3.* Section 4 introduces the positive POD algorithm to conduct phase field reconstruction. Section 5 applies the proposed algorithm to the *spectra of NiTiInol recorded in the scans along the tensile axis at different stages of loading.* Section 6 draws some conclusions.

2. Equi-atomic NiTiInol under uniaxial tensile loading

2.1. Tested specimen

A specimen of quasi-equiatomic Ni-Ti alloy (NiTiInol) (thin parallelepipedic central zone of length $L_{AD} = 14$ mm, width $l = 3$ mm and thickness $h = 0.3$ mm) is  (Figure 1)) in a mechanical testing machine located within the XRD chamber. The specimen surface is speckled with white paint to provide enough contrast for Digital Image Correlation (DIC) analyses to measure displacement field under load. Attention was paid to the fact that the paint did not affect the diffraction pattern over the range of diffraction angles of interest in the following.

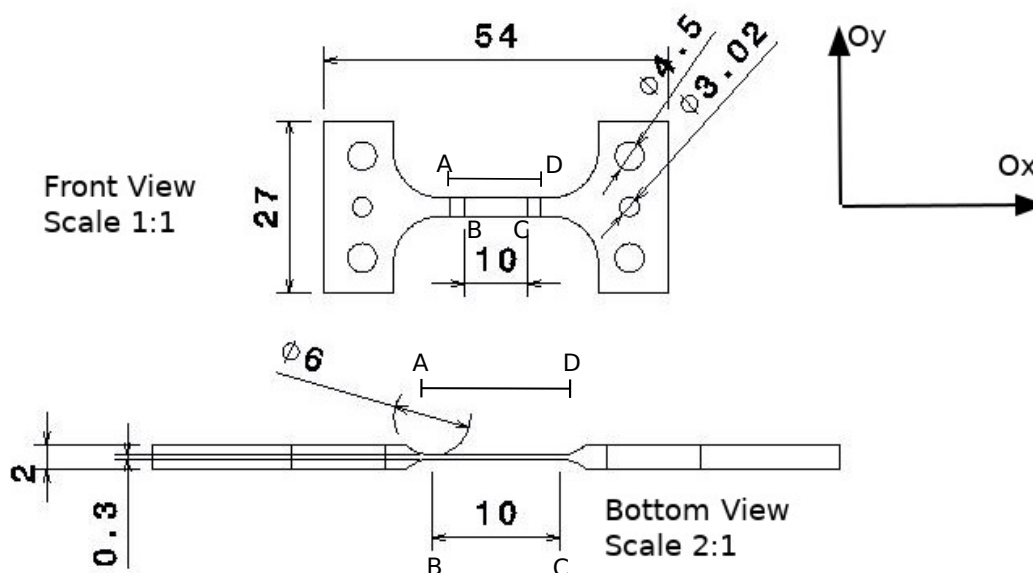


Fig. 1. Geometry of the specimen for uniaxial tensile test. The effective zone for XRD measurement is between A and D, of length $L_{AD} = 14$ mm.

2.2. Experimental setups

As shown in Fig. 2 and 3, the wide-angle X-ray diffractometer equipped with a conventional X-ray source (Cobalt K_{α} with a wavelength $\lambda = 1.79 \text{ \AA}$) and a curved detector (**Inel CPS-120**) is used to measure the X-ray diffraction spectrum along diffraction angle 2θ varying between $20^{\circ} < 2\theta < 140^{\circ}$. An Fe filter is used to suppress the contribution of Co K_{β} in X-rays radiation.

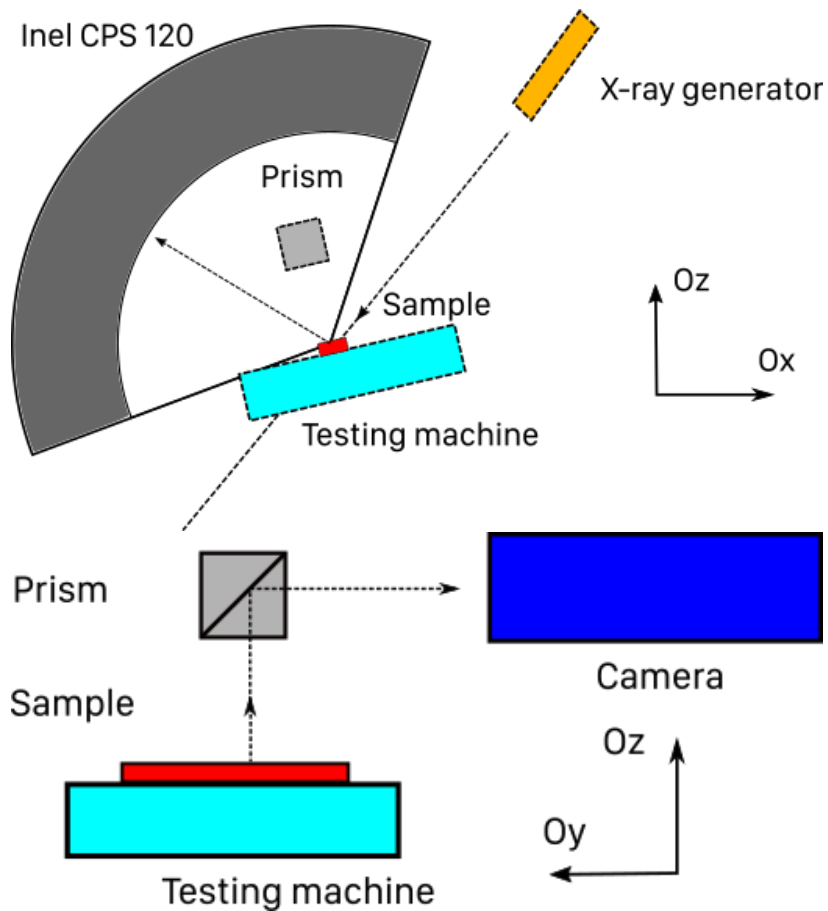


Fig. 2. Scheme of the in-situ combined multi-field measurement: XRD and Digital Image Correlation (DIC). (Top) Angular XRD measurement setup in the Oxz plane (Bottom) Schematic illustration of DIC setup in the Oyz plane.

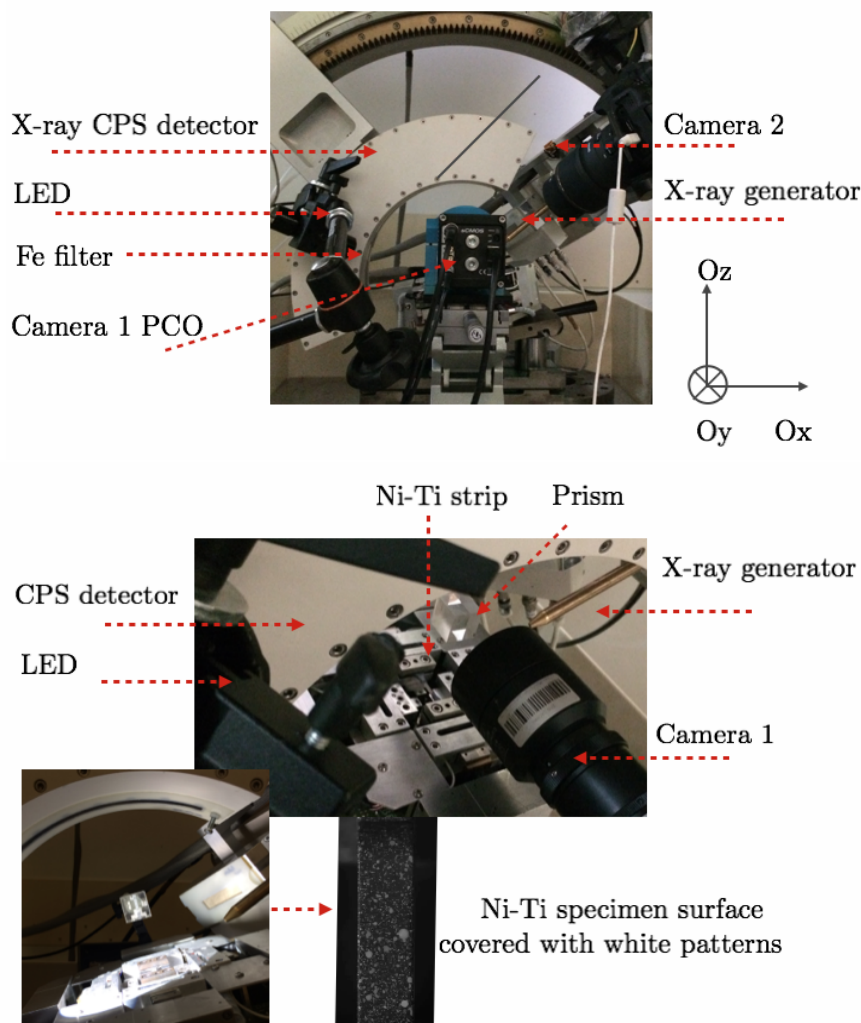


Fig. 3. Different views of in-situ combined XRD and DIC measurement setup

To limit any cross-influence between both setups, a *prism* is used to redirect the image of the specimen surface toward a visible-light camera (Camera 1). A displacement-controlled 1D tensile test is carried out at room temperature $T = 300$ K with a loading speed $\dot{U} = 1 \mu\text{m}\cdot\text{s}^{-1}$ (corresponding to a longitudinal strain rate $\dot{\epsilon} = 10^{-4} \text{s}^{-1}$). In the stress-free configuration, an initial XRD scan is conducted; then the mechanical test is interrupted three times along the loading stage, during which the displacement is held constant ($U = 0.3$ mm, 0.4 mm, 0.6 mm) and a similar hold time is considered at unloading ($U = 0.3$ mm) to perform the

XRD measurement along a longitudinal profile (referred to as a “scan” in the following). The corresponding stress / strain curve is reported in Fig 4(a). The DIC-measured deviatoric strain field and strain rate are plotted in Fig 4(b). Two localization bands are formed, the region where the strain is above 5%, corresponds to the region which has ~~been~~ transformed into martensite. The strain rate field highlights the transformation front. The temperature elevation due to the latent heat released in the phase transformation prevents the propagation of a single transformation front, hence several bands are observed in the tested specimen.

The geometry of the specimen is given in Fig.1. The designed region of interest is 10 mm long between points B and C, with B and C marked with very shallow landmarks. However, points B and C could no longer be seen during the experiment for both DIC and XRD measurements, after spraying the speckle patterns onto the specimen. As a result, the effective X-ray diffraction region length was 14 mm long, between point A ($x = 0$) and D ($x = 14$). At each of the four interruptions (denoted as Step # 0-3), (shown as red marks in Fig 4a), X-ray diffraction spectra are recorded, scanning along the load axis in the central part the Ni-Ti specimen (corresponding to the spatial scanning coordinates $0 \text{ mm} \leq y \leq 14 \text{ mm}$).

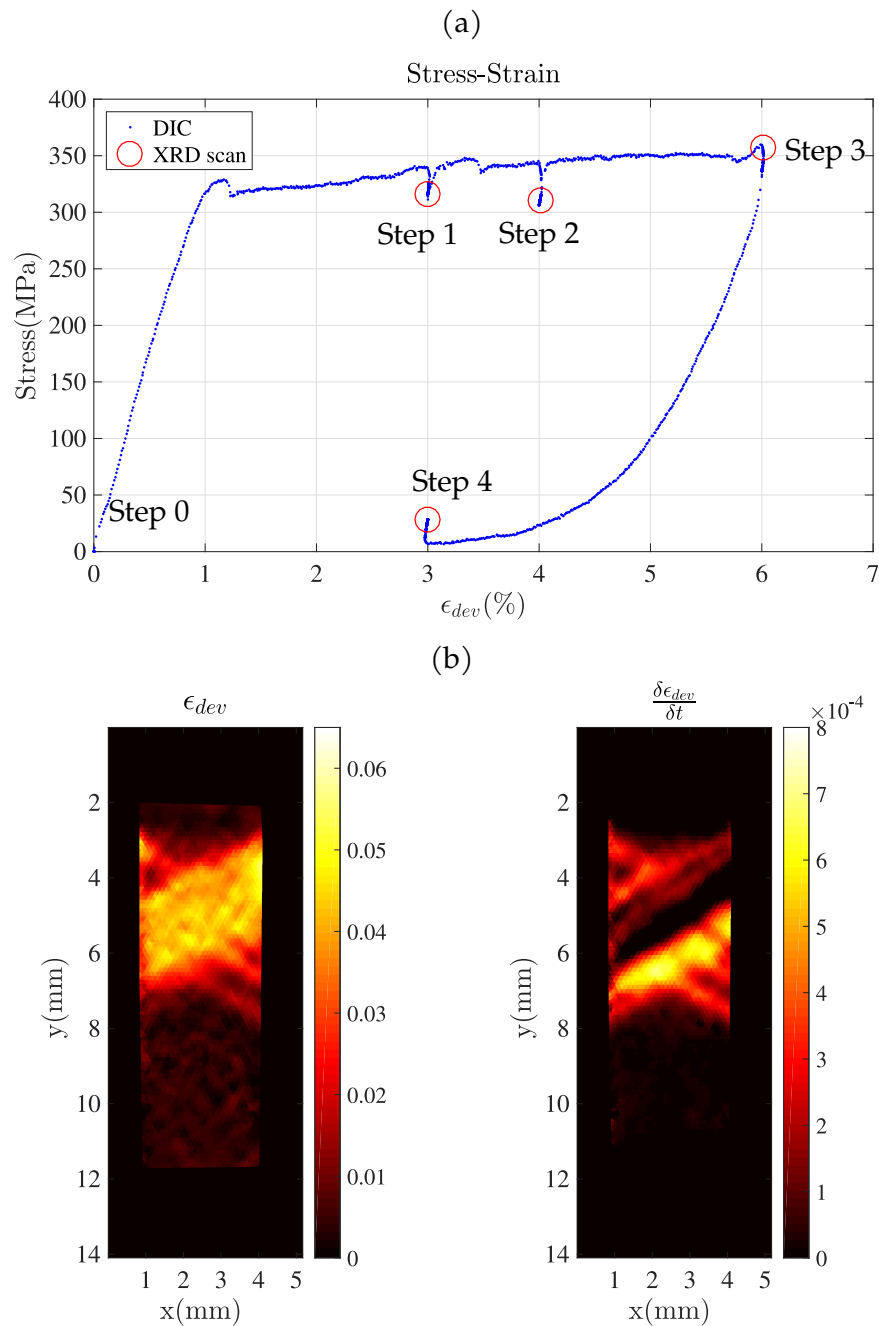


Fig. 4. (a) Stress-Strain curve during the 1D tensile load. The positions where the XRD scans are recorded are shown as red circles; (b) The (Eulerian) deviatoric strain (left) and strain rate (right) fields at the first loading stage (**Scan performed at Step # 1**), as measured by DIC, appear to be strongly heterogeneous.

2.3. Spatial spectra

The raw spectra collected at the four interruption stages are plotted in Fig 5. For the sake of readability, here and in the following, an offset proportional to the y coordinate of the studied spot is added to the spectra so that they do not overlap.

2.3.1. Masking and Clipping

As indicated in Fig 5, it should be emphasized that some angular intervals of the recorded spectra are not reliable:

- The contribution of Co K_{β} in experimental X-ray diffraction should be excluded.¹
- The Fe filter gives rise to a double absorption in the range of diffraction angles $62^{\circ} \leq 2\theta < 65^{\circ}$
- The optical prism obscures the X-rays detector for $2\theta \geq 100^{\circ}$ during Step 1-3², as shown in Fig 3

In order to properly perform the peak indexation of the diffractograms, masking all these three regions is mandatory. Consequently, all diffraction signals shaded in gray as shown in Fig 5, within the corresponding range of diffraction angles (that is $[44^{\circ}, 46^{\circ}] \cup [62^{\circ}, 65^{\circ}] \cup [100^{\circ}, 140^{\circ}]$), are discarded from the analysis throughout this paper.

¹ The exclusion of Co K_{β} grants us with a single dominant wavelength of λ to facilitate the indexation of diffraction peaks by using diffraction theory.

² During Step 0, the prism was not installed yet

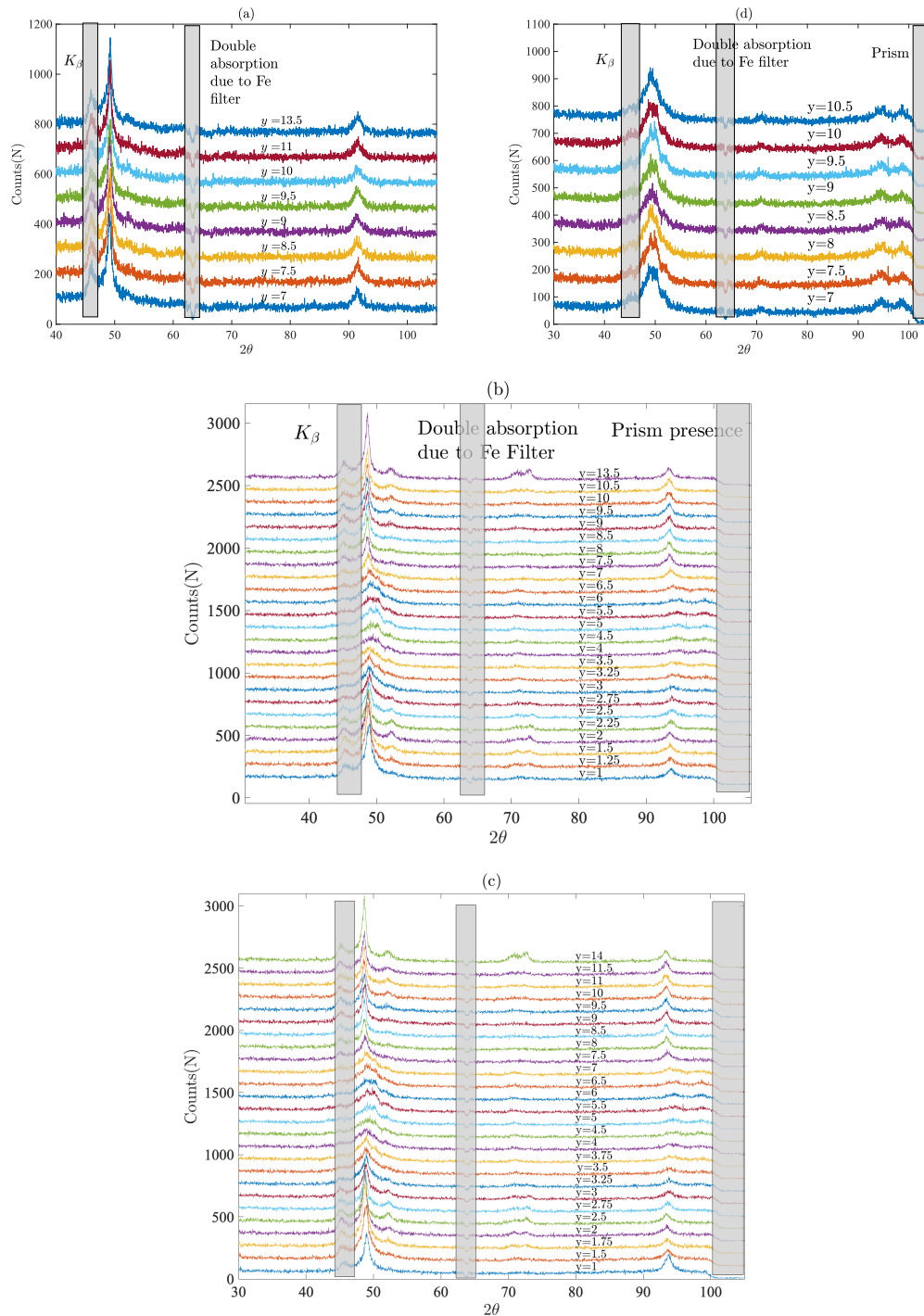


Fig. 5. Diffraction spectra at different spatial coordinates (a) Step 0: Stress-free state (b)-(c) Step 1-2: (intermediate stages) on-going martensitic transformation inside the region of interest (d) Step 3: (maximum displacement) the central zone of the sample is fully transformed into Martensite

2.3.2. *Qualitative analysis* The crystallography of NiTiInol alloys has been massively investigated. With the published crystallographic information (Austenite and Martensite (Bhattacharya, 2003) and R-phase (Zhang & Sehitoglu, 2004)), it is possible to use the powder diffraction theory (Cullity, 1956) to construct the theoretical diffractograms (as illustrated in Fig 6), and the qualitative characterization of the phase constituents present at the four different stages.

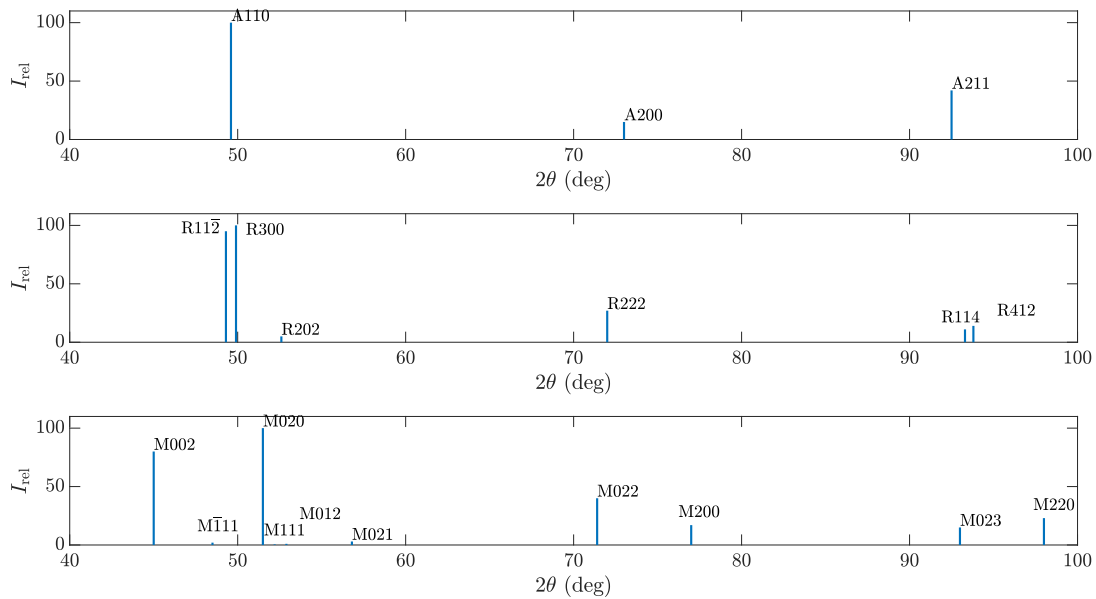


Fig. 6. Theoretical X-ray diffraction profiles (Integrated intensities) for Austenite, R phase and Martensite

- Step 0: At ambient load-free state ($\sigma = 0$ MPa, $T = 300$ K), NiTiInol is usually considered as pure Austenite. The $\{hkl\}$ diffraction peaks at different spatial coordinates in Fig 5(a) at $2\theta = 49^\circ$ and 92° correspond to $A\{110\}$ and $A\{211\}$, which are consistent with the theoretical X-ray diffraction diagrams. $\{200\}$ peak is not visible in the experimental spectra because of the pronounced crystallographic texture of this laminated material (Chang *et al.*, 2020). Therefore, at this stage, the collected experimental diffraction spectra are taken as the data profile for pure Austenite.

- Step 3: Experimental pure Martensite diffraction spectra can be collected when the external loading has reached the end of stress-strain transformation plateau — at the point “Step 3” marked with a red circle as shown in Fig 4. The corresponding diffractogram Fig 5(d) can be considered as pure Martensite with a typical double Martensite peak between $90^\circ \leq 2\theta \leq 100^\circ$.
- Step 1 and 2: When comparing the diffractograms at different spatial locations as illustrated in Fig 5(b)-(c), pronounced differences can be observed. For example, focusing on the range of $48^\circ \leq 2\theta \leq 52^\circ$, a large shift of the peak position and of its broadening characterized by its Full Width at Mid-Height (FWMH) can be seen along the sample axis. For all spectra acquired in the range $2\text{ mm} \leq y \leq 4\text{ mm}$ (within the high strain band as illustrated in Fig 4.b) the spectra appear as pure Martensite, characterized by their typical double Martensite peaks between $90^\circ \leq 2\theta_b \leq 100^\circ$. Outside the transformed region, the co-existence of Austenite and R-phase can be verified by the secondary peak at $2\theta = 51^\circ$ which can be unambiguously attributed to the R-phase $\{202\}$ crystal lattice diffraction plane.

From Fig 5, a series of raw spectra $\mathbf{D}(2\theta, y)$ is obtained, each of which is composed of the three phases of NiTiInol: Austenite (A), Martensite (M) and R-phase (R). For the proper identification of phases, it is possible to prepare the specimen to obtain pure A and M phases with either a load-free state at high temperature (Austenite), or under load after a full transformation (Martensite) with a representative anisotropy along the tensile axis due to the variants selection. However, it is not the case for R-phase: in a previous study (Chang *et al.*, 2020), by conducting a Differential Scanning Calorimetry measurement over the Nitinol specimen, it is shown that R phase is present only at intermediate stages, and never uniformly.

With a careful sequential Rietveld refinement, thermal-induced Martensite detwinning diffraction profiles and associated concentrations can be accurately estimated, as reported in the work of (Oliveira *et al.*, 2021). However, in the present case, the combination of the

missing knowledge of R-phase diffraction profiles and possible preferred-orientation effect due to 'Martensite detwinning', makes it very delicate to use the Rietveld refinement method to conduct any reliable quantitative analysis. To better highlight these difficulties, and how we propose to circumvent those difficulties with the "Positive POD" (or p-POD) algorithm, the Rietveld method and its limitations are briefly recalled in the following section.

3. Rietveld method

The original presentation of the Rietveld method (Rietveld, 1969) is followed in the sequel.

3.1. The integrated intensities and estimated diffraction profile

For Bragg diffraction peak, the integrated intensities, $I_{\{hkl\}}$, can be written as follows

$$I_{\{hkl\}} = K p_{\{hkl\}} L_{\theta} P_{\theta} A_{\theta} T_{\{hkl\}} E_{\{hkl\}} F_{\{hkl\}}^2 \quad (1)$$

where K is the scale factor; $p_{\{hkl\}}$ is the multiplicity factor to account for the symmetry in the reciprocal lattice; L_{θ} , P_{θ} , and A_{θ} represent respectively the Lorentz', the polarization, and the absorption factors; $T_{\{hkl\}}$ stands for the preferred orientation factor; $E_{\{hkl\}}$ designates the extinction factor; and $F_{\{hkl\}}$ the structure factor.

Various effects generate a Gaussian-like broadening of each peak, so that the estimated diffraction profile for a given pure phase α can be approximated as

$$\mathbf{S}_{\alpha}^{\text{calc}}(2\theta) = \sum_{\{hkl\}} I_{\alpha, \{hkl\}} \exp\left(-\frac{4 \ln(2)}{H_{\{hkl\}}^2} (2\theta - 2\theta_{\{hkl\}})^2\right) + \mathbf{D}_{\text{bg}}(2\theta) \quad (2)$$

where $H_{\{hkl\}}$ represents the full width at the half maximum (FWHM) for a given $\{hkl\}$ peak and $\mathbf{D}_{\text{bg}}(2\theta)$ represents the background of X-ray diffraction.

3.2. Rietveld refinement


Several assumptions are made here: diffraction profiles between different phase constituents follow a natural mixture law, and other X-ray diffraction parameters are known

(e.g., background, FWHM, asymmetry parameters, unit cell dimensions, preferred orientation, etc.). Rietveld refinement aims to determine the phase concentration through a non-linear least square fitting

$$\mathcal{C}_\alpha = \arg \min_{C_\alpha} \sum_{2\theta} \{ \mathbf{D}^{\text{exp}}(2\theta) - \sum_{\alpha} C_\alpha \mathbf{S}_\alpha^{\text{calc}}(2\theta) \}^2 \quad (3)$$

where \mathbf{D}^{exp} represents the experimental diffraction profile.

Despite the widespread usage of Rietveld refinement in X-ray diffraction characterization, three major limitations need to be specifically addressed:

1. Noise: the quadratic cost function implemented in Rietveld refinement rest upon the assumption that the noise in the X-ray diffraction measurement follows a Gaussian distribution with a uniform variance (in 2θ) for \mathcal{C}  optimal. However, for X-ray detectors, it is commonly reported that noise follows a Poisson distribution. In such a case, the chosen quadratic cost function in Rietveld refinement is not “wrong” but not optimal. Hence the nature of measured noise needs to be first characterized, and the cost function needs to be adapted accordingly, with a weight proportional to the inverse intensity.
2. Correlated parameter fitting: to the best of the authors’ knowledge, most commercial codes using Rietveld refinement require a sequence of parameter refinement (background, unit cell crystal parameters, asymmetry parameters, preferred texture factor, etc) to reach the sought phase concentration. Therefore, when dealing with data from a mixture of different phases with a pronounced texture preference, the non-linear least square fitting is prone to secondary minima trapping, and the set of correlated parameters (concentration, preferred orientation) are ill-estimated. Thus, simplifying the Rietveld refinement protocol and determining the phase concentration with fewer model parameters is appealing.
3. The effect of preferred orientation: this question is further discussed in [subsection 3.3](#).

3.3. The effect of preferred orientation

In this subsection, addressing the role of preferred orientation for a single phase, α , it is assumed that other parameters remain constant in the entire experiment.


3.3.1. Case 1: Single crystal If the crystal lattice orientation of the phase is unique and represented using a rotation quaternion denoted as n_1 , the diffraction profile is denoted as $\mathbf{S}_\alpha^{n_1}$, which can be seen as the set of intensities of the different $\{hkl\}$ Bragg diffraction peaks.

For a single crystal having a different crystal orientation, say n_2 , its diffraction profile is related to the former from a matrix transformation, $T(n_1, n_2)$, such that

$$\mathbf{S}_\alpha^{n_1} = T(n_1, n_2) \mathbf{S}_\alpha^{n_2} \quad (4)$$

3.3.2. Case 2: A single crystallographic phase with a strong texture When a strong texture is present in the tested specimen, it is possible to use a reduced basis, (n_1, n_2) , to represent the distribution of possible crystal lattice orientation. The concentration of any experimental diffraction profile from phase α , can be approximated with the corresponding diffraction profiles $(\mathbf{S}_\alpha^{n_1}, \mathbf{S}_\alpha^{n_2})$.

$$\begin{aligned} \mathbf{D}_\alpha &= \sum_i^2 \mathbf{S}_\alpha^{n_i} C_\alpha^{n_i} \\ \sum C_\alpha^{n_i} &= 1, C_\alpha^{n_i} \geq 0 \\ \mathbf{S}_\alpha^{n_i} &= \mathbf{S}_\alpha^{e_i} T(n_i, e_i) \end{aligned} \quad (5)$$

3.3.3. Case 3: A single crystallographic phase but following a statistical distribution of orientations for multiple grains  that only three directions (for example, one of the most conventional choice is the $\langle 100 \rangle, \langle 110 \rangle, \langle 111 \rangle$ orientation used for the Pole figure), are required to

map the entire crystal orientation of specimen. Consequently, as a natural expansion of [Equation 4](#), any experimental diffraction profile of the polycrystal can be expressed as a linear

combination

$$\mathbf{D}_\alpha = \sum_i^3 \mathbf{S}_\alpha^{e_i} C_\alpha^{e_i}, \sum C_\alpha^{e_i} = 1, C_\alpha^{e_i} \leq 0$$

where $\mathbf{S}_\alpha^{e_i}$ and $C_\alpha^{e_i}$ represent respectively the X-ray diffraction profile following a given direction of the crystallographic lattice plane e_i , and its associated concentration. $\{e_1, e_2, e_3\}$ represents any basis of the diffracting crystal plane orientation.

Several remarks are to be made here:

1. Equation 6 can be considered as the generalized formulation of the experimental diffraction profiles of a pure phase (either single crystal or polycrystal with a pronounced texture preference are its particular cases).
2. Hereafter, $\mathbf{S}_\alpha^{e_i}(2\theta)$, is used to represent the X-ray diffraction profile for a single phase with a particular orientation e_i (after the convolution accounting for instrumental acquisition). In this respect, other model parameters are no longer to be identified independently for phase concentration determination. Thus the number of unknowns in refinement is drastically reduced.
3. When the preferred orientation effect is present in the tested sample, it requires at least two (and at most three) sets of preferred orientation factors; hence two or three diffraction profiles for the same phase are needed to guarantee a trustworthy phase concentration estimation. The preferred orientation correction implemented in the Rietveld refinement method is a first-order correction considering the principal crystal lattice orientation.
4. Moreover, let us emphasize that the non-unicity of the (reduced) basis e_i is very beneficial. Taking highly textured specimen as an example, one could select any reduced basis (n_1, n_2) and its corresponding diffraction profiles $(\mathbf{S}_\alpha^{n_1}, \mathbf{S}_\alpha^{n_2})$ to calculate the corresponding amplitudes $(C_\alpha^{n_1}, C_\alpha^{n_2})$.

The positive POD algorithm is introduced in the following section, and a proof of concept is given to construct a reduced basis from experimental data.

4. p-POD algorithm

The analysis consists in 5 steps:

1. Correction of background contribution;
2. Evaluation of XRD acquisition noise;
3. Preparation of the experimental diffraction data for each constituting phase for which spectra are experimentally available;
4. Estimation of the optimal set of phase concentrations for each ‘known’ phase by enforcing positivity constraints;
5. Estimation of the diffraction profiles for the remaining phase constituent.

4.1. Background correction

In addition to the sought diffraction peaks, a non-zero background signal is present in all spectra as a result of diffuse scattering, and unavoidable experimental imperfections (Cullity, 1956). It is therefore necessary to estimate this background signal $\mathbf{D}_{\text{bg}}(2\theta, y)$ and subtract it from the raw spectra $\mathbf{D}_{\text{raw}}(2\theta, y)$ prior to any further analysis.

$$\mathbf{D}(2\theta, y) = \mathbf{D}_{\text{raw}}(2\theta, y) - \mathbf{D}_{\text{bg}}(2\theta, y), \forall y \in \mathbf{y} \quad (6)$$

A 4-th order polynomial function is chosen to account for the spectrum background. It should be such that the resulting $\mathbf{D}(2\theta, y)$ should always be ‘positive’ after the background removal. Thus \mathbf{D}_{bg} is computed from the minimization of the following cost function, \mathcal{C}

$$\mathcal{C} = \sum_{\theta} (\mathbb{P}(\mathbf{D}_{\text{bg}}(2\theta, y) - \mathbf{D}_{\text{raw}}(2\theta, y)))^2 - \beta \mathbf{D}_{\text{bg}}(2\theta, y), \forall y \in \mathbf{y} \quad (7)$$

where \mathbb{P} is the ‘positive part’ function ($\mathbb{P}(y) = y$ if $y \geq 0$, and $\mathbb{P}(y) = 0$ if $y < 0$), and β is a scalar. The “Penalty” term, $\sum_{\theta} (\mathbb{P}(\mathbf{D}_{\text{bg}}(2\theta, y) - \mathbf{D}_{\text{raw}}(2\theta, y)))^2$, promotes the positivity of $\mathbf{D}(2\theta, y)$ so that the background should remain below the raw spectrum, while the second term favors a high background, with a uniform “pressure”, β , to line up to the minimum values of the spectrum. Because of the presence of XRD noise, the chosen parameter β is to be set so that some negatives values are tolerated in the resulting signal $\mathbf{D}(2\theta, y)$ (after background correction). In quantitative terms, β is tuned so that the negative values in the residuals have a distribution compatible with the characterized Poisson noise (discussed in the following section). Because of the truncation to negative values, the mean square value of those negative residuals should be half the noise variance.

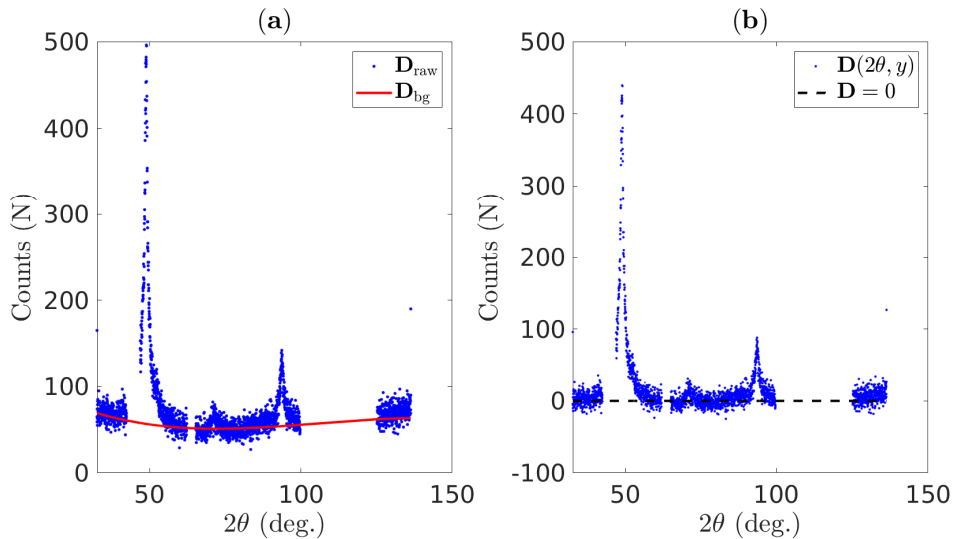


Fig. 7. (a) Raw diffraction spectrum plotted in blue and estimated background signal plotted in red (b) Corrected diffraction spectrum after background correction

In the following, a similar methodology is applied to determine the unknown R-phase spectrum : assuming that at this stage the Austenite and Martensite spectra are already known, by selecting the proper ratio between pressure and penalty terms, the Austenite/Martensite XRD contributions can be extracted from the experimental diffraction spectrum while the residual is

expected to be ‘positive’. Thus the residual can be further interpreted as the missing R-phase spectrum weighted by its concentrations.

4.2. Uncertainty analysis

In order to evaluate the noise associated to XRD analysis, it is proposed to conduct 5 scans over a single-phase specimen by varying the XRD acquisition time (*e.g.*, $t = 5, 10, 15, 20, 25$ min). Processing those acquisitions led to the conclusion that noise is Poisson-like, with a distribution that could not be distinguished from a Gaussian, and a variance that varies linearly with the mean count and thus the accumulation time. The motivation of this prior study is to allow assessing that the residual spectrum (difference between measured and estimated spectra) is compatible with the observed noise. In practice, this is done by estimating differences, and normalizing them (for all angles) by the local standard deviation (itself proportional to the square root of the mean signal and acquisition time). Comparing residual with noise thus consists in observing that this scaled residual is uniform over all angles, and its distribution is a Gaussian of zero mean and unit variance.

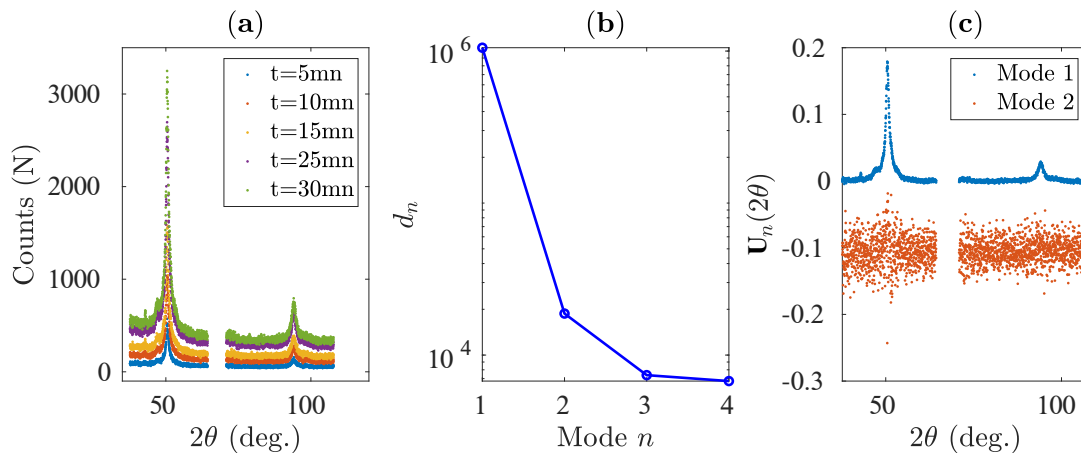


Fig. 8. Uncertainty analysis: (a) Experimental Austenite spectra collected with different acquisition times; (b) Eigenvalues of each POD modes ranked in decreasing order; (c) Angular shape functions for the first two POD modes. The second mode has been offset by -0.1 for readability

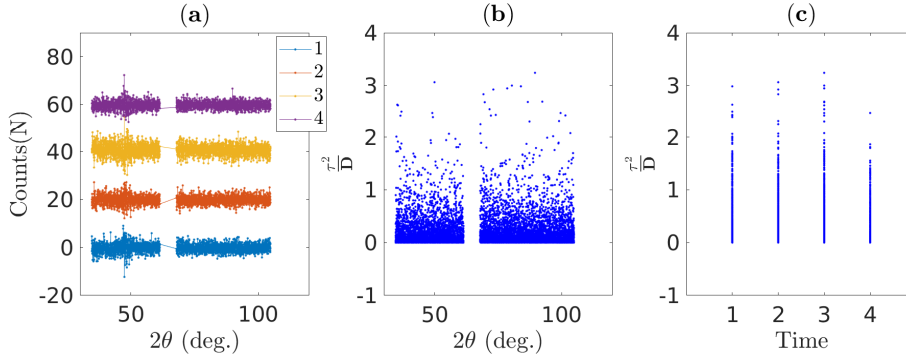


Fig. 9. (a) Characterized noise follows a Poisson-type distribution (b)-(c) Angular/Temporal stationarity for re-scaled noise τ^2/\mathbf{D} after Anscombe transformation

4.3. Experimental diffraction data for pure phase constituents

In order to collect pure diffraction data while taking potential preferred orientation effects into account, it is recommended to collect diffraction spectra at N different spatial coordinates y and rearrange them into a matrix form, $\mathbf{D}(2\theta, y)$, onto which a POD analysis is performed

$$\mathbf{D}(2\theta, y) = \sum_{n=1}^N d_n \mathbf{U}_n(2\theta) V_n(y) \quad (8)$$

where the $\mathbf{U}_n(2\theta)$ represents the n -th POD angular modes and $V_n(y)$ is the corresponding spatial amplitude, d_n represents the energetic contribution of n -th POD mode into the diffraction matrix, as a result of the normalization of each mode, $\|\mathbf{U}_n\|_{\theta} = 1$ and $\|V_n\|_y = 1$ (the subscript after the norm symbol recalls that these two norms operate in different spaces).

In the following, the discussed test case is such that three phases and only three are expected in this material. With the additional assumption that their orientation is **tr** **ly isotropic**, then it would be expected that no more than three modes are needed to account for the entire set of data. This obviously does not mean that the angular modes, $\mathbf{U}_n(2\theta)$ for $n = 1, 2$ or 3 , should coincide with pure phase spectra, but rather that the linear combinations of these three modes should be sufficient to match any composition of the three phases.

This simple presentation rests on the assumption of a unique type of orientation distribution

per phase. Here transverse isotropy is the most likely, but a single orientation, or an isotropic distribution would also lead to the same result that no more than three mode are needed to account for all acquired experimental spectra (at the exception of noise that can be considered as an additional mode). In the case where orientation, or orientation distribution is evolving along the loading, then more modes should be added with a maximum of three modes per phase, as above discussed (neglecting symmetries than can reduce this number).

It should however be emphasized that, one of the key properties of POD analysis is that modes are ordered along a specific hierarchy, according to their relative power contributions³ in decreasing order. Hence, the analysis has the potential to proceed with simple assumptions (such as no more than three modes), and test from the residuals (the unexplained data) whether they are compatible with noise and hence the initial three phase assumption is deemed satisfactory or if the basis should be enriched to account for preferential orientation effects. (Note that when the residual is within the noise level, it does not mean that the assumptions are correct, but simply that their further refinement can not be obtained from the currently available noisy XRD data). It is important also to stress that because modes are not spectra of pure phases, some work is needed to perform a physically meaningful conversion. This is the motivation of the following section.

4.4. Positive POD algorithm

For powders, any diffractogram obtained at a given spatial coordinate, $\mathbf{D}(2\theta, y)$, should be equal to the sum of each pure i phase spectrum $\mathbf{S}_i(2\theta)$ weighted by its volume fraction $C_i(y)$. For Austenite, due to its crystalline symmetry (with a BCC crystalline structure), its experimental XRD spectrum is unique regardless of its crystal orientation. On the contrary, assuming that R-phase and Martensite (with a much lower crystalline symmetry compared to Austenite) are subject to potential variant-selection during 1D tensile load; a different combi-

³ More precisely, the power of n -th mode is proportional to its squared eigenvalue, d_n^2 .

nation of variant-selection induces a modulation of different peak intensities for XRD spectra, consequently the experimental diffraction patterns for R-phase and Martensite are not unique

$$\mathbf{D}(2\theta, y) = \sum_{\alpha} C_{\alpha} \mathbf{S}_{\alpha} + \tau(2\theta), \alpha = A, R^i, M^j \quad (9)$$

$$\sum_{\alpha} C_{\alpha} = C_A(y) + \sum_i C_{R^i}(y) + \sum_j C_{M^j}(y) = 1, \quad \forall y \quad (10)$$

where $S_{R^i}(2\theta)$ denotes the i -th R-phase diffraction spectrum, $S_{M^j}(2\theta)$ represents the j -th Martensite phase diffraction spectrum and τ denotes the Poisson-noise of the raw signal.

As earlier discussed, the diffraction patterns for Austenite and Martensite variants can be experimentally obtained, whereas the R-phase diffraction profile is yet unknown. After eliminating the entire signal contribution from all 'known' phase constituents, $\sum_{\alpha} C_{\alpha} \mathbf{S}_{\alpha}$ (α denotes Austenite and Martensite spectrum), the remaining diffraction signal at any given diffraction angle is expected to remain *positive* for each angle. However, because of the presence of XRD noise, one may tolerate some negative values (as for the case of background signal removal) when consistent with our prior knowledge on its statistical characteristics.

In the following, at each position y , an optimum set of local phase concentrations $C_{\alpha}(y) = [C_A, C_{M^j}]$ can be obtained through the quadratic minimization of the primary cost function

$$\mathcal{F}(C_{\alpha}) = \sum_{2\theta} \mathbb{P} \left(\sum_{\alpha} C_{\alpha} \mathbf{S}_{\alpha}(2\theta) - \mathbf{D}(2\theta, y) \right)^2 - \sum_{\alpha} \beta_{\alpha} C_{\alpha} \mathbf{S}_{\alpha}(2\theta), \quad \alpha = A, M^j \quad (11)$$

where \mathbb{P} is the positive part function, and β_{α} is a positive scalar. Similarly to the background correction, the so-called ‘‘Penalty’’ term, $\sum_{2\theta} \mathbb{P} \left(\sum_{\alpha} C_{\alpha} \mathbf{S}_{\alpha}(2\theta) - \mathbf{D}(2\theta, y) \right)^2$, promotes the positivity of the residual signal, $\rho(2\theta, y) = \mathbf{D}(2\theta, y) - \sum_{\alpha} C_{\alpha} \mathbf{S}_{\alpha}(2\theta)$ so that the total contribution of all known phase constituents, $C_{\alpha} \mathbf{S}_{\alpha}$, should remain below the local diffraction signal. In contrast, the second ‘pressure’ term, $\sum_{\alpha} \beta_{\alpha} C_{\alpha} \mathbf{S}_{\alpha}(2\theta)$, favors a large contribution for each known constituent, which is increased as much as possible (similar to the ‘penalty’ and ‘pressure’ terms introduced for the background).

It also should be emphasized that the minimization of the primary cost function should be carried out under the following convex inequalities constraints:

- Each phase concentration is expected to be positive,

$$C_\alpha(y) \geq 0, \quad \alpha = A, M^j \quad (12)$$

- The sum of all concentrations is expected to be lower than 1.

$$C_A(y) + \sum_j C_{M^j}(y) \leq 1, \quad \forall y \quad (13)$$

In the following, it is proposed to group all the above physical inequalities constraints on the concentrations(12- 13) into a single matrix form

$$\mathbf{EC} - \mathbf{F} \geq 0 \quad (14)$$

4.5. Sub-gradient projection

Finding the optimum set \mathbf{C} with respect to all positive constraints is a typical convex inequality constrained problem, which consists in minimizing the cost function, $\mathcal{F}(\mathbf{C})$, subject to $\mathbf{EC} - \mathbf{F} \geq \mathbf{0}$. The sub-gradient projection method is frequently used to handle constrained optimization problem. First, the dual cost function (or the so-called Augmented Lagrangian), $\mathcal{G}(\mathbf{C}, \lambda)$, is introduced

$$\mathcal{G}(\mathbf{C}, \lambda_L) = \mathcal{F}(\mathbf{C}) + \lambda_L(\mathbf{EC} - \mathbf{F}) \quad (15)$$

where λ_L is the classical Augmented Lagrange multiplier to ensure that all physical concentrations constraints are fulfilled. The minimization of the dual cost function not only pushes the residual ρ close to 0 while remaining 'positive', but also grants the physical admissibility of phase concentrations.

With an initial guess of $\mathbf{C}^{(k)}$, the sub-gradient can be computed

$$\mathbf{T}^k(\mathbf{C}^{(k)}, \lambda_L) = [\partial_{\mathbf{C}^{(k)}} \mathcal{G}, \partial_{\lambda_L} \mathcal{G}]^\top \quad (16)$$

Here $\mathbf{T}^k(\mathbf{C}^{(k)}, \lambda_L)$ is a positive and monotonous operator. The solution $\mathbf{C}^{(k)}$ is updated via the sub-gradient projection.

$$\mathbf{C}^{(k+1)} = \mathbf{C}^{(k)} - \eta \mathbf{T}^k \quad (17)$$

where η is the step length. A relatively small step length is applied to prevent numerical oscillations, $\eta = 1$. The value of η could be further optimized for a faster convergence rate. However, because computation time was not critical, this optimization was not investigated. The sub-gradient projection is repeated until $\mathbf{C}^{(k)}$ reaches a stationary value

$$\left| \frac{\mathbf{C}^{(k+1)} - \mathbf{C}^{(k)}}{\mathbf{C}^{(k)}} \right| \leq 10^{-4} \quad (18)$$

It should be emphasized that sub-gradient method is not a descend method, the primal and dual cost function values can (and often do) increase before reaching convergence.

5. Positive POD algorithm applied to the case of nickel titanium alloys

5.1. Background correction

One example of background correction procedure is illustrated in Fig 7 using a local spectrum at step 1. The missing channels due to experimental artifact (K_β , double absorption of Fe filter, prism obscuration), makes the 4-th order polynomial background signal fitting even more difficult. To overcome this problem, it is proposed to add additional information of diffraction signals over $2\theta \in [35^\circ, 45^\circ] \cup [125^\circ, 135^\circ]$, which are away from any relevant diffraction peaks; and these channels are expected to be centered around zero after the background removal. The presence of 'zero' channels at the boundary of spectrum instead of diffraction peaks, improves greatly the stability of background correction algorithm.

After choosing the proper ratio $\beta = 0.12$ between the pushing force and the penalty term (see Equation 7), the background signal has been properly estimated (after background correction, for 2θ channels away from $\{hkl\}$ diffraction peaks, the diffraction counts are mostly centered at 0). The differences between the background signals at different spatial positions are very small, therefore the average of background signal was used in this study to minimize uncertainty. In the following of this section, for all four loading stages where XRD scan have been carried out, raw diffraction spectra have received the same background removal as a pre-processing before launching the p-POD analysis.

5.2. Uncertainty analysis

The uncertainty analysis is carried out over the fully austenitic NiTiInol at room temperature. Five XRD scans are carried out with corresponding acquisition time intervals $t = 5, 10, 15, 25, 30$ min (Fig 4.2a) and the differences between each XRD scan are then computed (Fig 4.2b).

The identified noise follows a Poisson-type distribution (the variance scales with the amplitude of the diffraction signals at each channel, see Fig 9a). When a signal is affected by a Poisson noise, its Anscombe transform exhibits a stationary Gaussian noise of uniform variance (Anscombe, 1948) as soon as the noise amplitude is small compared to the signal. In the present case, the Anscombe transform simply consists in taking the square root of the signal. The re-scaled noise after Anscombe transformation indeed shows the expected variance uniformity over angle and time (see Fig 9b and c respectively).

5.3. Experimental diffraction data collection

5.3.1. Austenite diffraction spectrum After a thermal heating to completely transform the 1D NiTiInol strip into full Austenite state, the experimental Austenite diffraction data can be collected in the stress-free state at room temperature at 8 different spatial locations (as shown in Fig 5a). The POD analysis (Figure 10) indicates that for Austenite diffraction profiles, the first POD mode with highest eigenvalue can be interpreted as the diffraction pattern of Austenite and higher order POD modes (without any significant peak or structure) are **compatible with noise, and will be treated as such in the following.**

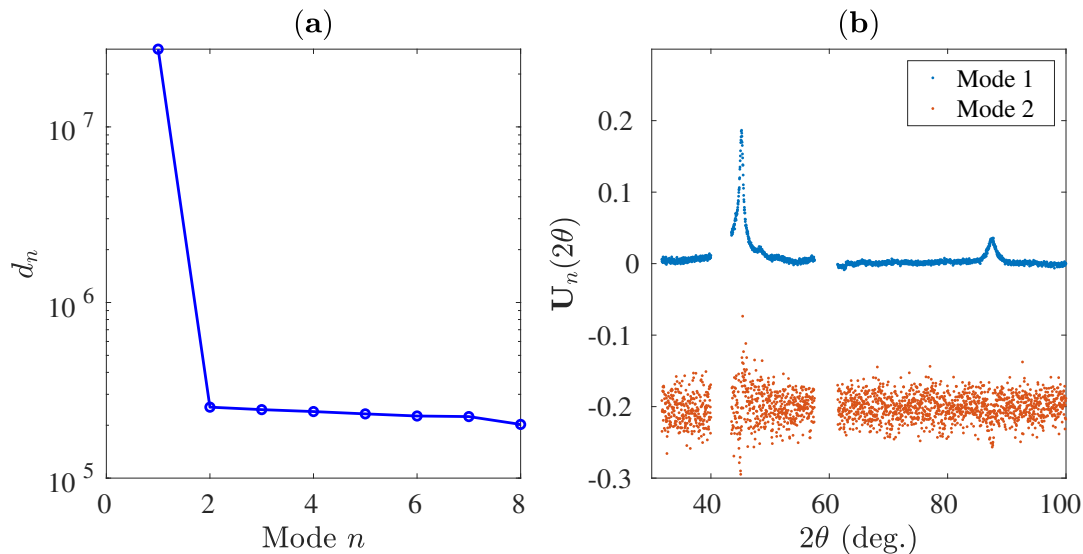


Fig. 10. POD analysis applied to the Austenite diffraction matrix (a): eigenvalue of each POD mode ranked in decreasing order (b): first two POD angular modes.

5.3.2. *Experimental Martensite diffraction spectra collection* The experimental Martensite diffraction data can be collected when the NiTiInol specimen has been fully transformed into Martensite (*e.g.*, the end of transformation plateau corresponding to **Step #3** in Fig 4(a)). In order to take into account potential preferred orientation effect, spectra are acquired at 8 different spatial coordinates in the region of interest ($y = 7, 7.5, 8, 8.5, 9, 9.5, 10$ and 10.5 mm). After rearranging the 8 different diffraction spectra into a matrix form, a POD analysis is performed (see Fig 11). Plotting eigenvalues against POD modes, it is clear that at least two POD modes are needed to faithfully describe all spectra.

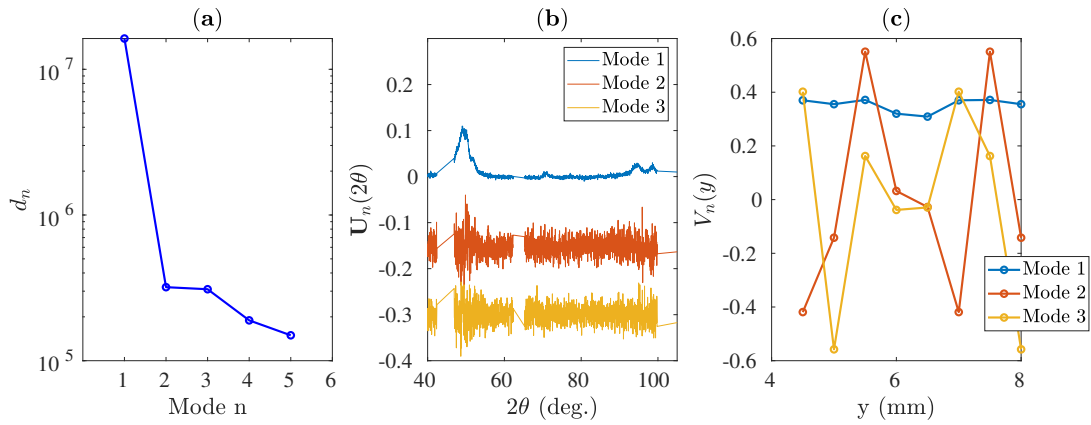


Fig. 11. POD analysis applied to experimental Martensitic diffraction spectra (a) : eigenvalue of each POD mode ranked in decreasing order; (b) The first three POD modes are shown. For clarify, successive modes are offset by -0.15; (c) first three spatial POD modes, $V_n(y)$, as a function of the spatial coordinate y .

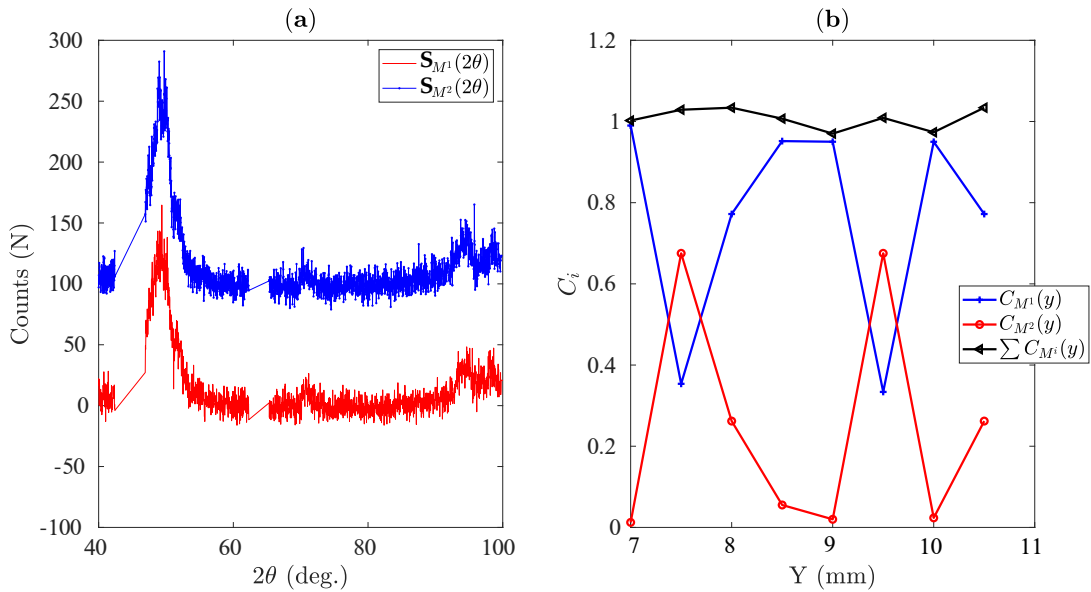


Fig. 12. (a) Two proposed set of different Martensite diffraction patterns where an offset of 100 counts is applied at S_{M^1} for readability; (b) Associated phase concentrations for two different martensite spectra at different spatial coordinates

The 1st POD angular mode represents the principal diffraction pattern of Martensite. In

the range $48^\circ \leq 2\theta \leq 53^\circ$, multiple Martensite diffraction peaks do contribute: $M\{\bar{1}11\}$

($2\theta = 48.3^\circ$), $M\{020\}$ ($2\theta = 51.4^\circ$), $M\{111\}$ ($2\theta = 52.4^\circ$) and $M\{012\}$ ($2\theta = 52.9^\circ$). In the range $92^\circ \leq 2\theta \leq 98^\circ$, one finds the characteristic Martensite diffraction peaks $M\{023\}$ ($2\theta = 93.4^\circ$) and $M\{220\}$ ($2\theta = 98.9^\circ$). Meanwhile higher order POD modes, even though very noisy, can be seen as the underlying undulation in $\{hkl\}$ intensities due to spatial heterogeneity of 'martensite detwinning' across the Martensite localization band.

When confronted with the non-unicity of Martensite diffraction data due to 'Martensite detwinning', it is possible to enrich the Martensite diffraction profiles by introducing multiple different Martensite diffraction patterns. In the present case, two Martensite patterns were chosen. The optimum set of two Martensitic diffraction spectra ($\mathbf{S}_{M^1}(2\theta), \mathbf{S}_{M^2}(2\theta)$) should satisfy the constraint of *physical admissibility*, namely, the corresponding phase concentration for each diffraction profile should obey

$$\mathbf{D}(2\theta, y) = C_{M^1}(y)\mathbf{S}_{M^1}(2\theta) + C_{M^2}(y)\mathbf{S}_{M^2}(2\theta) + \tau(2\theta, y) \quad \forall(2\theta, y) \quad (19)$$

$$C_{M^1}(y) + C_{M^2}(y) \leq 1, \quad \forall y \quad (20)$$

One possible example set (this set is not unique) ($\mathbf{S}_{M^1}(2\theta), \mathbf{S}_{M^2}(2\theta)$) is illustrated in Fig 12(a). The first experimental Martensite diffraction spectrum promotes the $M\{020\}$ diffraction peak while the second shows an enhanced intensity for the $M\{111\}$ peak. The two proposed Martensite diffraction data consistently represent the entire diffraction matrix, given that the overall sum of these two phase constituents at different spatial coordinates y equals almost 1 while each individual concentration remains physically admissible. The reason for which the sum of concentrations does not strictly equals 1 may be due to the fact that two spectra are not enough to exhaustively describe the Martensite orientations, but the residual data is so small that adding a third phase would make the problem much less robust, and it was decided not to enrich this description.

Note that the experimental profiles for Austenite and Martensite are now set to the above spectra, $\mathbf{S} = [\mathbf{S}_A(2\theta), \mathbf{S}_{M^1}(2\theta), \mathbf{S}_{M^2}(2\theta)]$. Hence hereafter it is possible to estimate the optimum set of phase concentration for Austenite and Martensite for **Step #1** and **#2** in Fig 4(a)

and eventually characterize the R-phase diffraction spectrum and its concentration.

5.4. Positive POD algorithm applied to scans #1 and #2

Two local spectra are selected as examples to illustrate the performance of the proposed algorithm. The first spectrum, \mathbf{D}_{12} , is selected for an acquisition positioned inside the transformed bands (with the presence of a strongly preferred orientation effect) while the second spectrum, \mathbf{D}_4 , is selected at a point which is located at the interface between the Austenite matrix and a Martensite band.

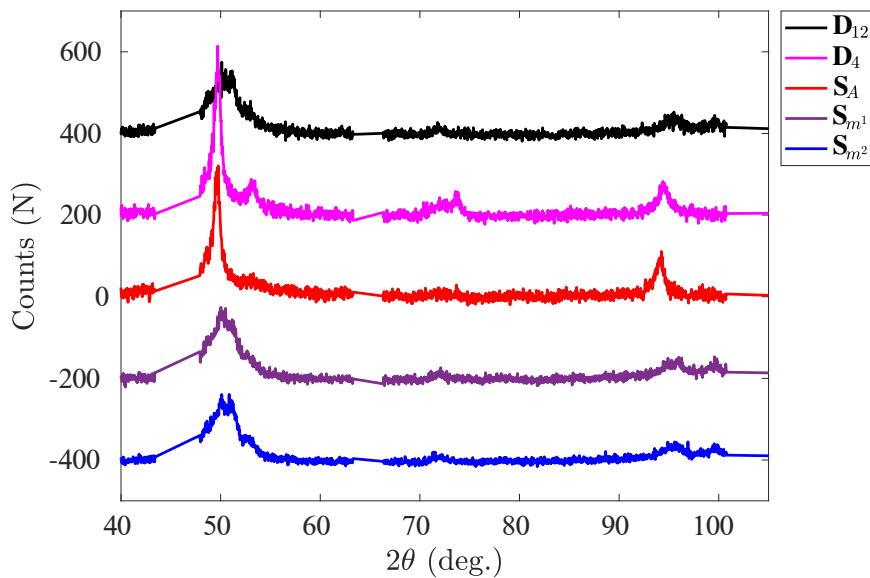


Fig. 13. Two investigated local XRD scans and known XRD diffraction data for Austenite and Martensite, each spectrum has been offset by 200 counts for readability

5.4.1. *First case: Acquisition within the transformed band* At convergence of the p-POD algorithm where both the primal and dual cost functions reach a stationary value (Fig 14(b)), each constituent concentration is physically admissible and they sum up to a value close to 1 ($\sum C_\alpha \simeq 0.95$, see Fig 14(a)). Furthermore, the final residual almost vanishes when compared to the initial spectrum. When re-scaled by the standard deviation of XRD noise, it does not show any significant angular dependency. Thus it can be concluded that the p-POD algorithm

is reliable and efficient to account for the preferred orientation effect by introducing physical constraints and two representative Martensite diffraction patterns.

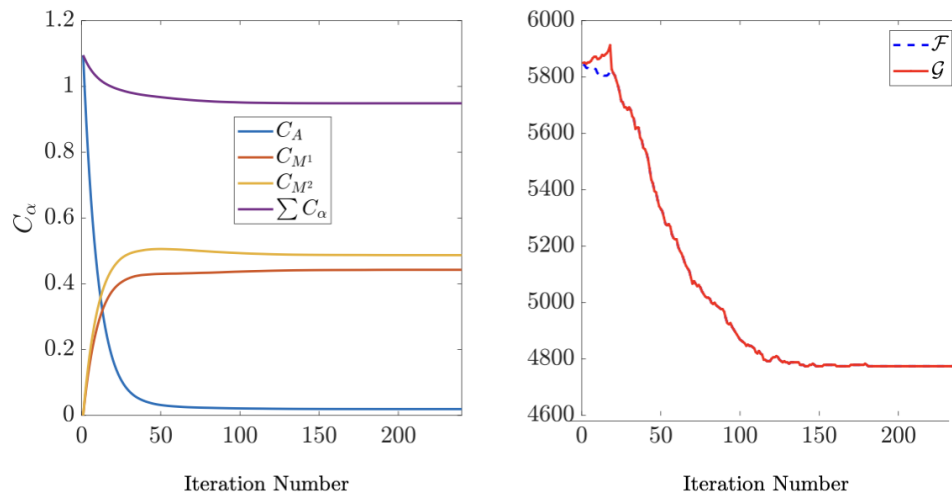


Fig. 14. (a) Phase concentrations for Austenite and Martensite constituents (b) The primal/dual cost functions against iteration number

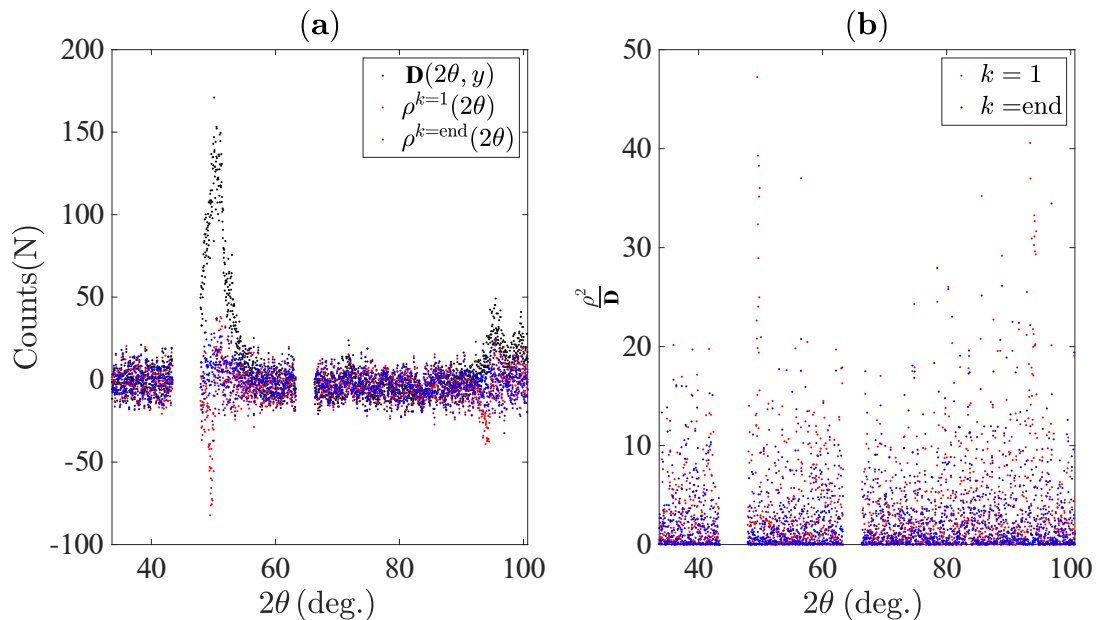


Fig. 15. (a) Comparison between raw spectrum, initial residual and final residual (b) Initial and final re-scaled residual

5.4.2. Second Case: Acquisition at the interface between matrix and transformation band In the second case, the Austenite and Martensite concentrations stabilize at convergence (see Fig 16) where the sum is well below 1 (0.6). The remaining signal after removing Austenite and Martensite contributions (Fig 17(a)), still shows a pronounced angular dependency after Anscombe transformation that cannot be attributed to noise. After considering the locations of the diffraction peaks, and their indexation, it is concluded that they do correspond to the R-phase.

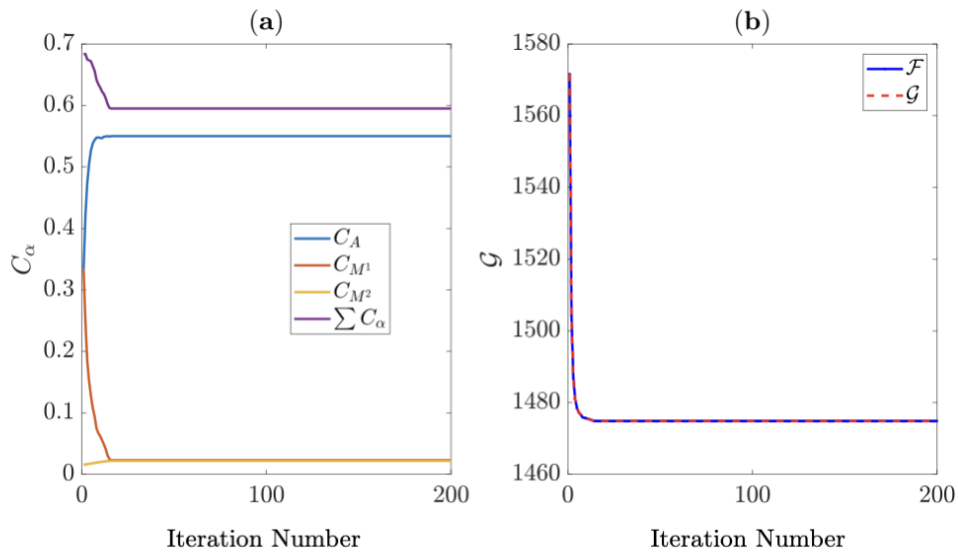


Fig. 16. (a) Phase concentration for Austenite and Martensite (b) Primal/Dual cost function against the iteration number

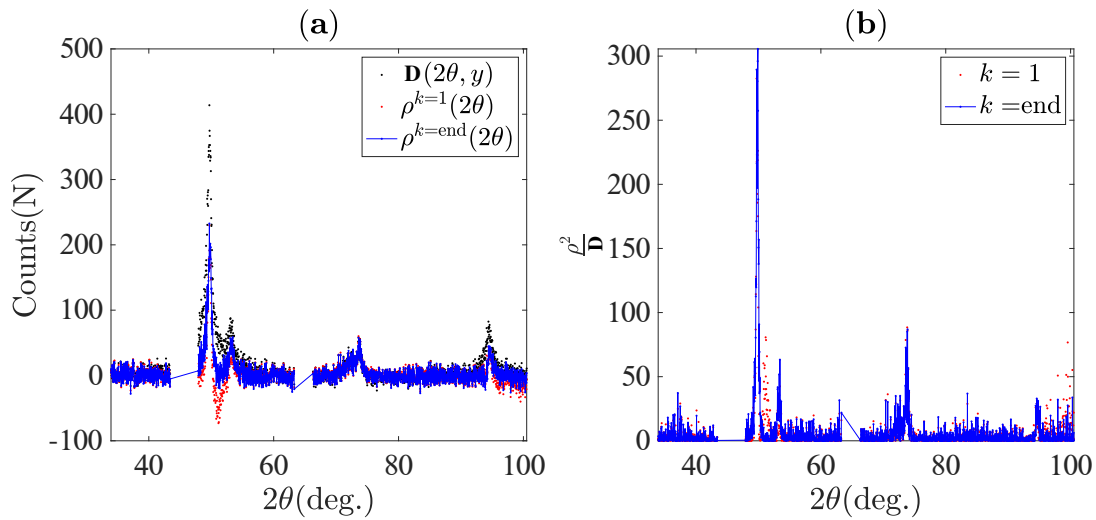


Fig. 17. (a) Comparison between the raw spectrum, initial and final residual (b) Re-scaled residual

5.4.3. R-phase diffraction pattern reconstruction The p-POD algorithm is applied to the entire set of spectra collected during scan 1. After removing the diffraction contributions from Austenite and Martensite, the residual, (remaining signal), $\rho(2\theta, y)$ in the diffraction signal is displayed in Fig 18(a). A POD analysis over $\rho(2\theta, y)$ shows that at least two POD modes are required to account for the remaining diffraction signal (Fig 18(b)). The first POD angular mode corresponds consistently with R-phase powder diffraction peaks, with features such as a double peak (R $\{11\bar{2}\}$ and R $\{112\}$) at $2\theta = 49.3^\circ$ and $2\theta = 49.6^\circ$, several secondary diffraction peaks R $\{202\}$ at $2\theta = 52.7^\circ$, or R $\{222\}$ at $2\theta = 73.6^\circ$. Meanwhile higher order POD modes can be seen as underlying $\{hkl\}$ intensity undulations due to heterogeneous R-phase detwinning at different spatial positions (Fig 18(c)-(d)).

Similarly to the case of Martensite detwinning, it is possible to use two different R-phase diffraction patterns to take into account a preferred orientation effect (see Fig 19a). The two R-phase diffraction profiles correspond well to the theoretical R-phase diffraction peaks, but with different $\{hkl\}$ peak weights. With the complete diffraction pattern, the phase concentrations for each constituent as functions of the scan position are illustrated in Fig 19b. All concentrations are always bounded between [0,1], and their sum never exceeds 1. At several points, where the sum of concentrations is slightly less than 1 (~ 0.95), it can be inferred that detwinning introduces multiple R-phases and Martensite diffraction patterns (not only limited to 2). Additional R-phase and Martensite diffraction profiles could be further introduced to improve phase field reconstruction, but the small signal-to-noise ratio becomes limiting.

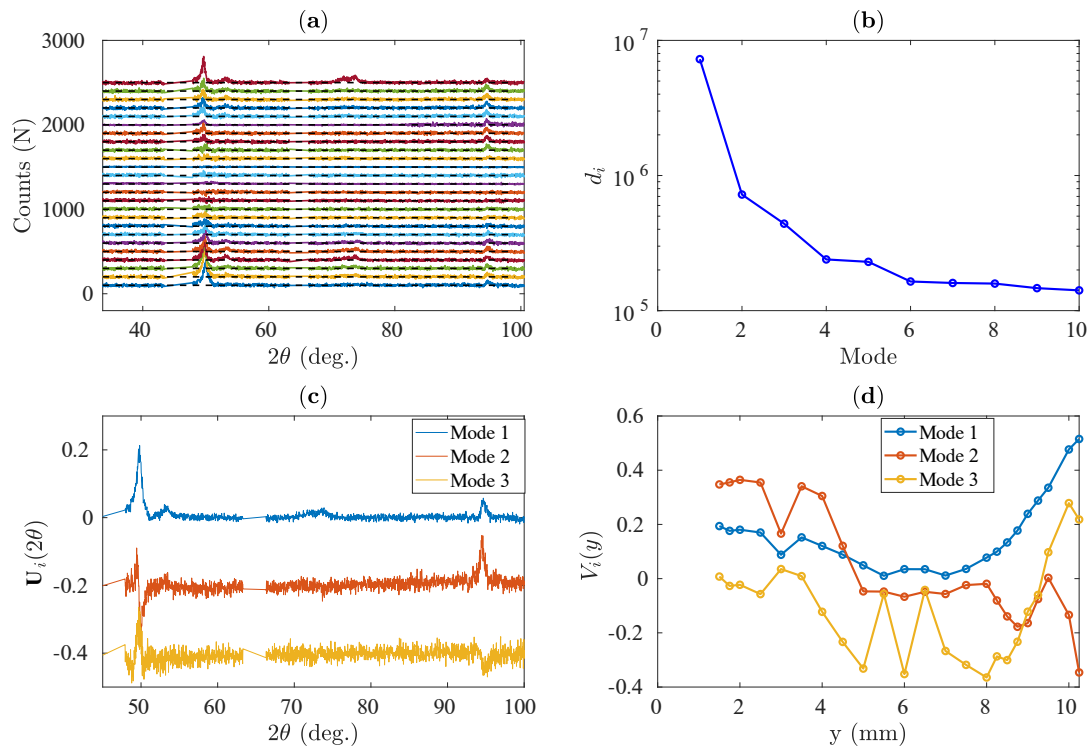


Fig. 18. POD analysis applied at ρ : (a) Residual diffraction signal after removing Austenite and Martensite contributions (b) Eigenvalues of each POD mode ranked in decreasing order (c) First three POD angular modes (d) First three POD spatial modes

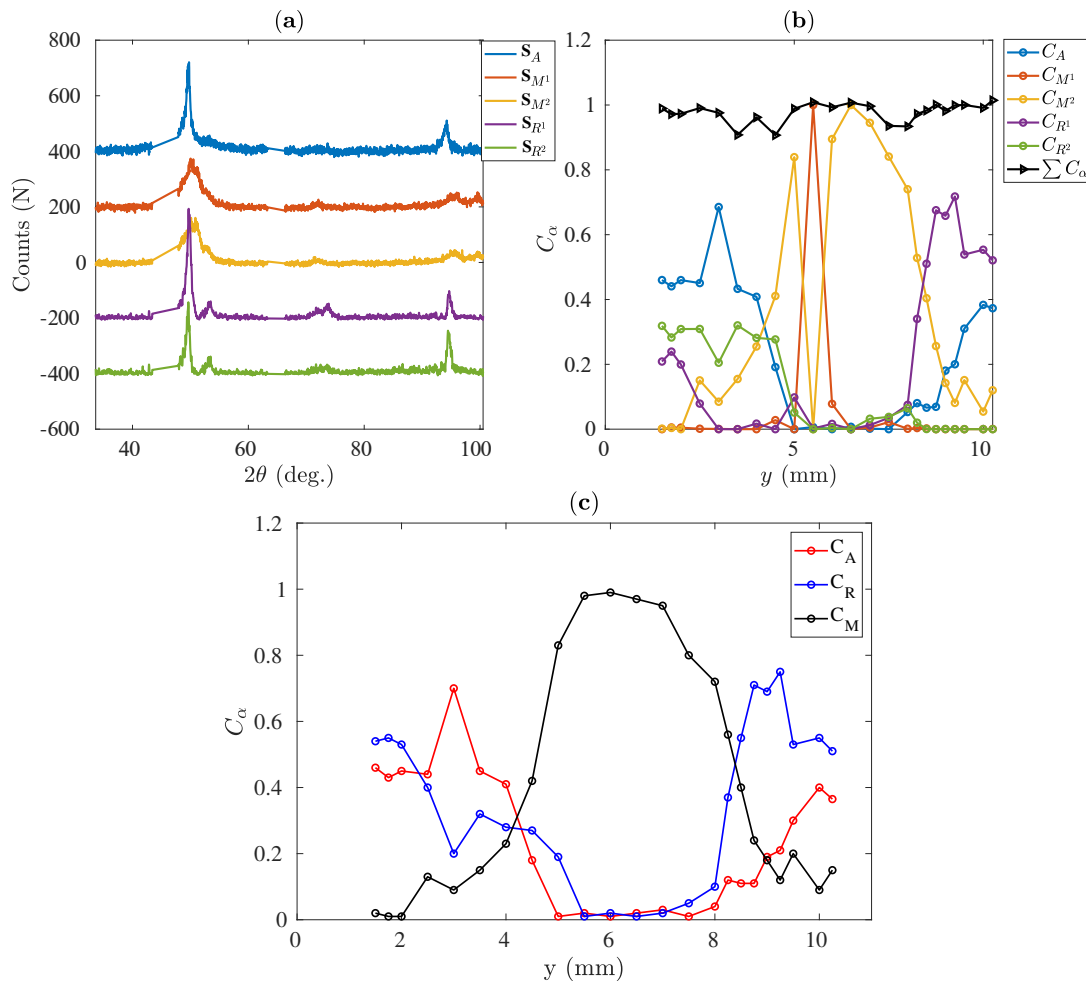


Fig. 19. (a) The diffraction patterns for Austenite, R-phase and Martensite, each has been offset by 200 for readability (b) The phase concentration for each constituent at different spatial positions (c) The phase concentration for A, R, M at different spatial positions.

Fig. 19 (c) shows that the central part of the specimen has been transformed to martensite almost completely, whereas the ends are composed of a mixture of A and R-phase. Thus it appears that from pure Austenite, a R-phase is nucleated under load, coexisting with the Austenite, and these two phases eventually turn completely into Martensite. This is consistent with the DSC characterization where A is transformed into M in a two step process with an R-phase as an intermediate phase because of the thermal heterogeneity during 1D tensile load.

6. Conclusions

Quantitative XRD analysis remains a great challenge when aiming to a quantitative evaluation of heterogeneous materials. Classical Rietveld method and its generalizations are not adequate when dealing with incomplete database of diffraction patterns for each phase constituent, or undetermined spatial heterogeneous texture distribution for one or several constituents.

When assessing a pure phase with strong spatial heterogeneity in texture distribution, instead of using one unique artificial texture as implemented in the March model, the proposed approach used Proper Order Decomposition to capture the diffraction patterns at different spatial coordinates. This allowed for the reconstruction of one or several experimental diffraction patterns, which are much more flexible to account for the entire diffraction spectra including limited orientation modulations.

Moreover, by including inequality constraints into convex minimization, the herein introduced ‘positive-POD’ algorithm can seamlessly remove diffraction contributions from known phase constituents and make it possible to reconstruct diffraction patterns for the unknown constituent afterwards. Additionally, the accuracy of the reconstructed unknown constituent can be justified by powder diffraction indexation. This algorithm, can be considered as a step forward compared to the March model. Its extreme versatility appears as a promising tool in quantitative XRD analysis for complex heterogeneous materials.



1. Crystal orientation of equiatomic NiTiInol

As shown in Figure 20, the equiatomic Nitinol exhibits a very pronounced anisotropy in its crystal lattice orientation, as due to its lamination. The texture orientation is along the $\langle 111 \rangle$ direction, underlining its transverse isotropic texture.

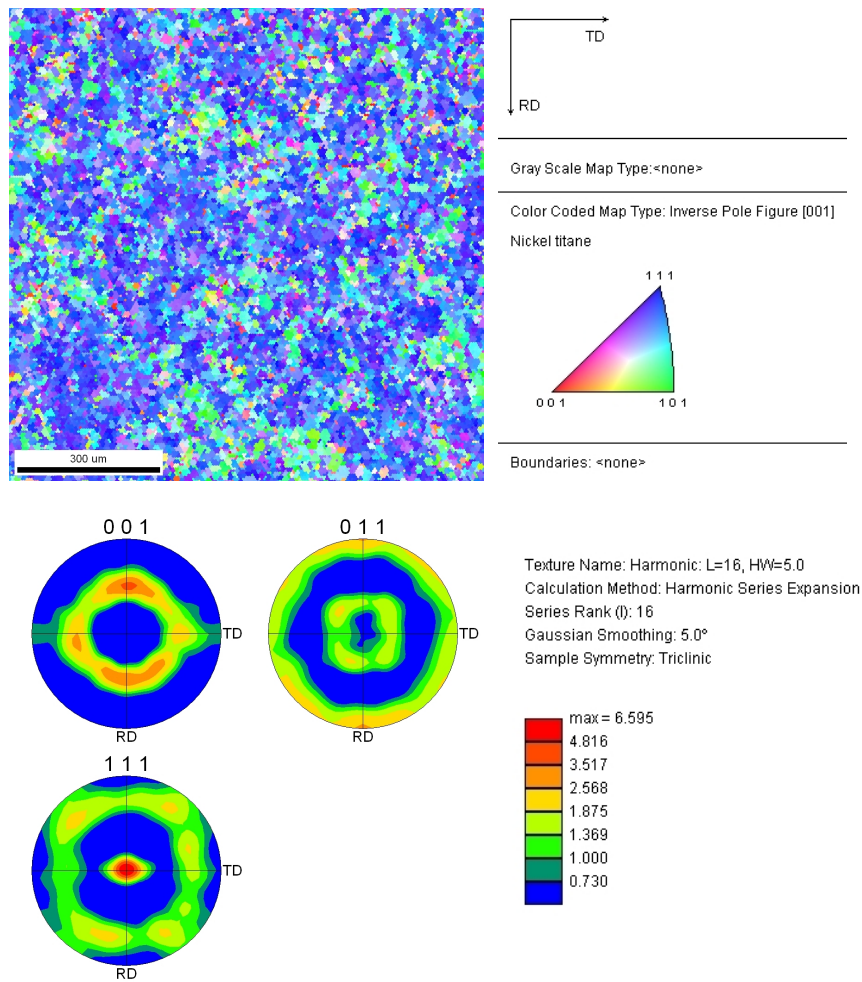


Fig. 20. Inverse pole figure (top) and pole figure (bottom) for the equiatomic Nitinol

2. The Differential Scanning calorimetry

The differential scanning calorimetry measurement of equi-atomic NiTiInol is shown in Figure 21. The presence of R-phase is manifest along cooling as an intermediate step between Austenite and Martensite.

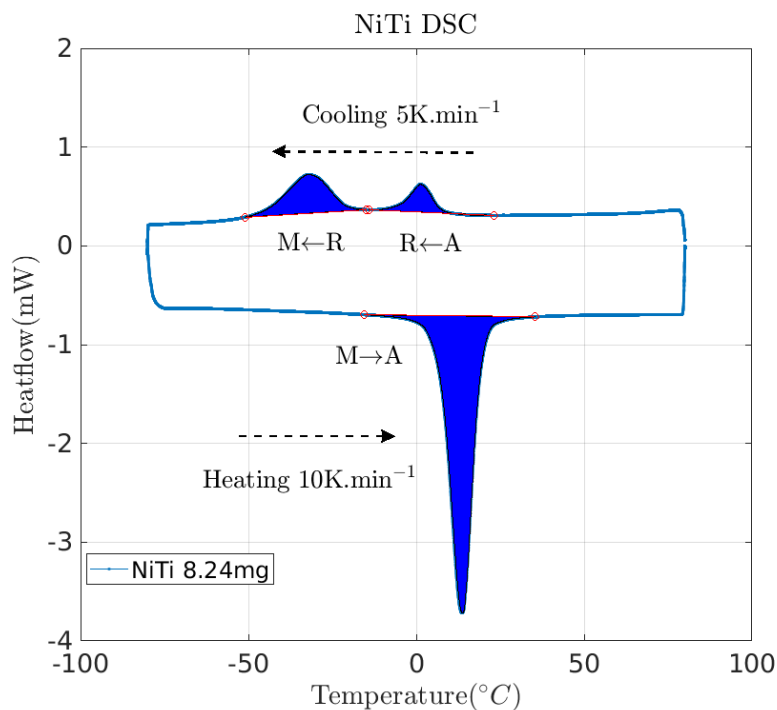


Fig. 21. DSC measurement, the two-step phase transformation during thermal loading confirms the presence of R-phase.

Acknowledgements

The authors thank Dr. Mame Daro Fall for discussions and Mr. Marc Bonnet for his technical support. XC wants to specially thanks the Ecole Normale Supérieure Paris-Saclay for financing his PhD grant.

References

- Anscombe, F. J. (1948). *Biometrika*, **35**(3/4), 246–254.
 URL: <http://www.jstor.org/stable/2332343>
- Bhattacharya, K. (2003). vol. 2.
- Boyd, S., Xiao, L. & Mutapcic, A. (2003). *lecture notes of EE392o, Stanford University, Autumn Quarter, 2004*, 2004–2005.
- Campbell Roberts, S. N., Williams, A. C., Grimsey, I. M. & Booth, S. W. (2002). *Journal of Pharmaceutical and Biomedical Analysis*, **28**(6), 1149–1159.
 URL: <https://www.sciencedirect.com/science/article/pii/S0731708502000535>
- Chang, X., Lavernhe-Taillard, K. & Hubert, O. (2020). *Mechanics of Materials*, **144**, 103361.
 URL: <https://www.sciencedirect.com/science/article/pii/S0167663619308567>
- Chatterjee, A. (2000). *Current Science*, **78**(7), 808–817.
 URL: <http://www.jstor.org/stable/24103957>
- Cullity, B. D. (1956). *Elements of X-ray Diffraction*. Addison-Wesley Publishing.

- Dickson, M. J. (1969). *Journal of Applied Crystallography*, **2**(4), 176–180.
URL: <https://doi.org/10.1107/S0021889869006881>
- Dollase, W. A. (1986). *Journal of Applied Crystallography*, **19**(4), 267–272.
URL: <https://doi.org/10.1107/S0021889886089458>
- Drickamer, H., Lynch, R., Clendenen, R. & Perez-Albueene, E. (1967). vol. 19 of *Solid State Physics*, pp. 135–228. Academic Press.
URL: <https://www.sciencedirect.com/science/article/pii/S0081194708605299>
- Gailhanou, M., Loubens, A., Micha, J.-S., Charlet, B., Minkevich, A. A., Fortunier, R. & Thomas, O. (2007). *Applied Physics Letters*, **90**(11), 111914.
URL: <https://doi.org/10.1063/1.2713335>
- Halani, P. R., Kaya, I., Shin, Y. C. & Karaca, H. E. (2013). *Materials Science and Engineering: A*, **559**, 836–843.
URL: <https://www.sciencedirect.com/science/article/pii/S0921509312013457>
- McCusker, L. B., Von Dreele, R. B., Cox, D. E., Louër, D. & Scardi, P. (1999). *Journal of Applied Crystallography*, **32**(1), 36–50.
URL: <https://doi.org/10.1107/S0021889898009856>
- Miyai, K., Ebihara, A., Hayashi, Y., Doi, H., Suda, H. & Yoneyama, T. (2006). *International Endodontic Journal*, **39**(2), 119–126.
URL: <https://onlinelibrary.wiley.com/doi/abs/10.1111/j.1365-2591.2006.01055.x>
- Ng, K. & Sun, Q. (2006). *Mechanics of Materials*, **38**(1), 41–56. Macro-, Meso-, Micro- and Nano-Mechanics of Materials.
URL: <https://www.sciencedirect.com/science/article/pii/S0167663605000852>
- Oliveira, J., Shamsolhodaei, A., Shen, J., Lopes, J., Gonçalves, R., de Brito Ferraz, M., Piçarra, L., Zeng, Z., Schell, N., Zhou, N. & Seop Kim, H. (2022). *Materials Design*, **219**, 110717.
URL: <https://www.sciencedirect.com/science/article/pii/S0264127522003392>
- Oliveira, J., Shen, J., Escobar, J., Salvador, C., Schell, N., Zhou, N. & Benafan, O. (2021). *Materials Design*, **202**, 109533.
URL: <https://www.sciencedirect.com/science/article/pii/S0264127521000861>
- Peng, L., Yajiang, L., Haoran, G. & Juan, W. (2005). *Materials Letters*, **59**(16), 2001–2005.
URL: <https://www.sciencedirect.com/science/article/pii/S0167577X05001692>
- Rietveld, H. M. (1969). *Journal of applied Crystallography*, **2**(2), 65–71.
- Sitepu, H., O'Connor, B. H. & Li, D. (2005). *Journal of Applied Crystallography*, **38**(1), 158–167.
URL: <https://doi.org/10.1107/S0021889804031231>
- Stebner, A. P., Paranjape, H. M., Clausen, B., Brinson, L. C. & Pelton, A. R. (2015). *Shape Memory and Superelasticity*, **1**(2), 252–267.
URL: <https://doi.org/10.1007/s40830-015-0015-2>
- Xiao, L. & Boyd, S. (2004). *Systems & Control Letters*, **53**(1), 65–78.
- Zhang, X. & Sehitoglu, H. (2004). *Materials Science and Engineering A-structural Materials Properties Microstructure and Processing - MATER SCI ENG A-STRUCT MATER*, **374**, 292–302.

Synopsis

Supply a synopsis of the paper for inclusion in the Table of Contents.
